Progress In Electromagnetics Research, Vol. 158, 73–87, 2017

Antenna Calibration Method for Dielectric Property Estimation of Biological Tissues at Microwave Frequencies

David C. Garrett*, Jeremie Bourqui, and Elise C. Fear

Abstract—We aim to estimate the average dielectric properties of centimeter-scale volumes of biological tissues. A variety of approaches to measurement of dielectric properties of materials at microwave frequencies have been demonstrated in the literature and in practice. However, existing methods are not suitable for noninvasive measurement of *in vivo* biological tissues due to high property contrast with air, and the need to conform with the shape of the human body. To overcome this, a method of antenna calibration has been adapted and developed for use with an antenna system designed for biomedical applications, allowing for the estimation of permittivity and conductivity. This technique requires only two calibration procedures and does not require any special manufactured components. Simulated and measured results are presented between 3 to 8 GHz for materials with properties expected in biological tissues. Error bounds and an analysis of sources of error are provided.

1. INTRODUCTION

The estimation of dielectric properties of materials at microwave frequencies has been investigated for numerous applications. Dielectric properties are used in biomedical applications ranging from assessment of tissue and device heating in magnetic resonance imaging [1] to radio frequency (RF) dosimetry [2] and improving microwave images by determining the signal speed within tissues such as the breast [3] or head [4]. Recent studies also suggest that microwave properties may be used to assess parameters such as human bone health [5] and hydration status [6].

The dielectric properties of biological tissues at microwave frequencies are most commonly estimated using open-ended coaxial probes, which perform local surface measurements. This method is reliable for homogenous materials where good contact with the material can be achieved, such as liquids and semi-solids [7]. Studies have reported the dielectric properties of *ex vivo* biological tissues including a variety of human and animal tissues [8]. However, these properties can change after excision due to water loss and temperature change [9], and tissue blood flow is not considered. Further, due to its shallow sensing depth, the open-ended coaxial probe is of limited use for noninvasive *in vivo* measurements where it is suitable only for surfaces such as the skin and tongue. Other methods of dielectric property estimation exist such as resonant cavity, transmission line, and free-space techniques, but these are impractical for *in vivo* tissues due to specific manufacturing requirements of the samples. We are interested in estimating the average properties of centimeter-scale volumes of tissues. We note that this bulk property estimation is of interest because *in vivo* measurements inherently consist of numerous biological tissues, where isolation of a single tissue is generally not possible. Bulk property estimates are useful in microwave imaging applications as prior information [10], as well as for evaluating tissue property variations when exploring new biomedical applications [11].

Received 22 December 2016, Accepted 8 February 2017, Scheduled 9 April 2017
* Corresponding author: David C. Garrett (dgarrett@ucalgary.ca).
The authors are with the Department of Electrical and Computer Engineering, Schulich School of Engineering, University of Calgary, Canada.

In order to estimate bulk permittivity of biological tissues, a method [12] has been developed that incorporates shielded, dielectrically-loaded ultra-wideband (UWB) antennas [13] in contact with tissues. The shielded antennas in proper contact allow for effective coupling of energy into the tissue, and minimize the unwanted path around the tissue. The bulk permittivity is estimated from the time necessary for the microwave signal to be transmitted through the tissue. However, no estimation of conductivity is obtained, and a second measurement without the tissue present is needed to determine time of arrival through the tissue.

In order to estimate both permittivity and conductivity over a range of frequencies, it is proposed to implement a method of antenna calibration to this system. This system is chosen due to its tailored design for biological tissue measurement and its UWB capabilities, providing a strong platform for property estimation. This paper aims to provide a novel technique of dielectric property estimation suitable for *in vivo* biological tissue assessment. With the ultimate objective of estimating bulk properties in heterogeneous tissues, this paper first aims to validate our technique using homogeneous samples. While developed for a particular UWB antenna, the method is anticipated to apply to other antenna designs operating in contact with tissues. We aim for an accuracy of 10% in order to be comparable with existing methods such as the open-ended probe [14], and to estimate background properties in microwave breast radar imaging where accuracy of approximately 10–20% is required for proper image reconstruction [15].

Several methods of microwave device calibration exist in literature. Thru-Reflect-Line (TRL) calibration [16] is commonly used for microstrip devices and has been adapted for free-space measurements [17]. However, for free-space applications, the Line measurement requires precise positioning equipment, and focusing lenses are often used to account for the signal's geometric spreading [18]. For the UWB antennas used in this study, the Line measurement requires a manufactured dielectric segment since the antennas are dielectrically-loaded. This could introduce error by manufacturing imprecisions and improper placement between the antennas. Thru-Reflect-Match (TRM) has also been proposed as a free-space calibration method, but is difficult to implement due to imperfections in absorbing layers used in the Match measurement, leading to residual errors [19].

A more recently developed calibration technique, Gate-Reflect-Line (GRL), is proposed in [20] as an improved method of free-space antenna calibration. GRL requires only two calibration measurements, which are performed at the same separation distance. This calibration procedure has been adopted in several commercially-available devices, and applied in a small number of studies such as [21]. Because of its reported superior property estimation accuracy in [20] and its lack of required manufactured components, GRL is chosen to be adapted for use with our system. An important distinction from the original GRL method is the location of the calibration planes, which are placed such that they enclose the material under test (MUT). Since the antennas used in this study are in direct contact with the MUT, it is desirable to place the calibration planes at the interface of the apertures of the antennas with the MUT. To account for this, the Reflect and Line measurements are modified. A second distinction from the original publication is a different method of dielectric property estimation from the calibrated signals, where the Nicolson-Ross Weir (NRW) method [22] is applied here.

In this paper, the calibration methodology is first presented in Section 2.1, focusing on differences from the original GRL publication. This is followed by its application in simulation and measurement in Sections 2.2 and 2.3, including the estimation of dielectric properties from the calibrated signals from 3 to 8 GHz. A comparison of simulated and experimental results is presented in Section 3 for the estimation of the dielectric properties of liquids with properties expected in biological tissues. This is followed by an analysis of sources of errors in Section 4. Finally, concluding remarks are given in Section 5.

2. METHODOLOGY

2.1. Calibration Method Overview

Two 2×2 matrices denoted $\mathbf{O}$ and $\mathbf{P}$ are used to characterize the two antennas. The matrices consist of complex values at each frequency point. Although the transmitting antenna differentiates the signal in the time domain [23], each frequency point is treated independently during calibration. A model of this system as well as the corresponding signal flow graph are shown in Figure 1. Note that the name of

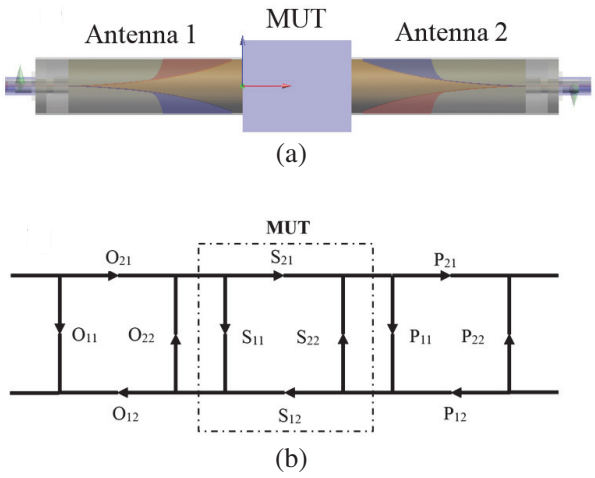

Figure 1. (a) System model in simulation. (b) Signal flow graph used for calibration.

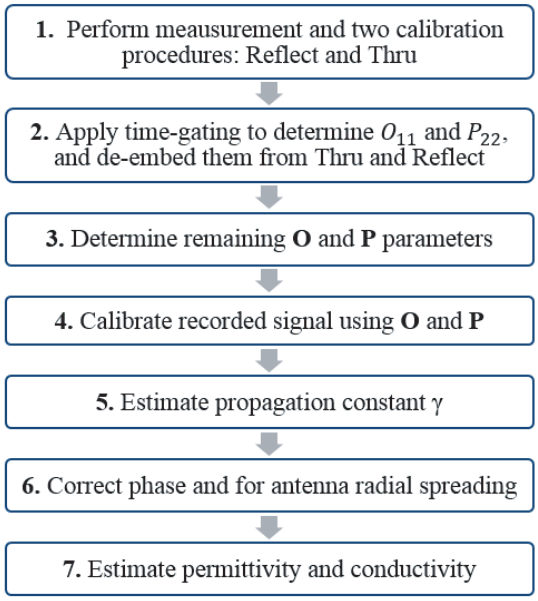

Figure 2. Flow chart describing GRL calibration and dielectric property estimation process.

the parameters has been modified from [20]. Radial spreading is not included in the signal flow graph, but is accounted for later by a gain correction factor.

The parameters of **O** and **P** as depicted in the signal flow graph are described as follows:

- O_{11} & P_{22}: reflections during transmission,
- O_{21} & P_{12}: losses and phase shift during transmission,
- O_{12} & P_{21}: losses and phase shift during reception,
- O_{22} & P_{11}: reflections during reception.

The antennas are modeled as reciprocal, with $O_{12} = O_{21}$ and $P_{12} = P_{21}$. Parameters O_{11} and P_{22} are obtained using time-gating to isolate reflections due to each antenna while transmitting, as will be demonstrated in detail alongside simulated results in Section 2.2. These parameters are then de-embedded from the calibration measurements. The remaining parameters can then be determined from the two calibration measurements, Reflect and Line. Finally, the response of the MUT can be extracted by removing the influence of the **O** and **P** matrices on measured S-parameters.

The GRL approach is modified here to allow for samples in contact with the antennas. The original publication describing GRL calibration performed free-space measurements of large planar samples, where horn antennas remained at fixed positions on either side of the sample [20]. The measurement system used in this study consists of two UWB shielded antennas, which are placed in direct contact with the material under test (MUT) [13]. To place the calibration planes enclosing the MUT at the antenna aperture, the Reflect procedure is performed with the antennas directly in contact with a planar perfect electric conductor (PEC) or metal sheet. The Line of the original GRL calibration is replaced with Thru where the antennas are directly in contact. For this reason, we name this calibration method Gate Reflect Thru (GRT).

For the Reflect procedure, it is assumed that the S-parameters at the antenna-PEC interface provide a perfect reflection and no transmission. Applying Mason's rule [24] to the signal flow graph (after de-embedding O_{11} and P_{22}):

$$Refl_{11} = -\frac{O_{21}O_{12}}{1+O_{22}} \tag{1}$$

$$Refl_{22} = -\frac{P_{12}P_{21}}{1+P_{11}} \tag{2}$$

where $Refl_{11}$ and $Refl_{22}$ are the reflection coefficients recorded at the first and second antenna terminals, respectively.

Next, the Thru measurement is performed with the two antennas directly in contact with one another. The S-parameters at this interface ideally result in a perfect transmission and no reflection. Note that mutual coupling between antennas is not accounted for due to the separation between antenna radiating elements. However, this should be considered when applying this technique to other antenna designs. Analysis of the signal flow graph results in:

$$Thru_{11} = \frac{O_{21}O_{12}P_{11}}{1 - P_{11}O_{22}} \tag{3}$$

$$Thru_{22} = \frac{P_{12}P_{21}O_{22}}{1 - P_{11}O_{22}} \tag{4}$$

where $Thru_{11}$ and $Thru_{22}$ are the reflection coefficients recorded at the first and second antenna terminals, respectively.

Solving for $O_{21}O_{12}$ and $P_{12}P_{21}$ in Eqs. (1) and (2) and substituting into Eqs. (3) and (4), respectively, yields:

$$Refl_{11}P_{11} + (Refl_{11} - Thru_{11})O_{22}P_{11} + Thru_{11} = 0 \tag{5}$$

$$Refl_{22}O_{22} + (Refl_{22} - Thru_{22})O_{22}P_{11} + Thru_{22} = 0 \tag{6}$$

Solving for P_{11} in Eq. (5) leads to:

$$P_{11} = \frac{-Thru_{11}}{O_{22}(Refl_{11} - Thru_{11}) + Refl_{11}} \tag{7}$$

Substituting Eq. (7) into (6) yields:

$$\begin{aligned} &Refl_{22}(Refl_{11} - Thru_{11}){O_{22}}^2 \\ &+[Refl_{11}Refl_{22} - Thru_{11}Refl_{11} + Thru_{22}Refl_{11}]O_{22} + Thru_{22}Refl_{11} = 0 \end{aligned} \tag{8}$$

This results in a quadratic equation to solve for O_{22} with two possible solutions. Since a passive antenna cannot have a reflection coefficient greater than 1, the correct solution can be determined. It is then possible to determine the remaining parameters using Eqs. (7), (1), and (2).

With the $\mathbf{O}$ and $\mathbf{P}$ matrices determined, the calibrated S-parameters can be obtained. The signal flow graph from Figure 1 involves three cascaded matrices, so T-parameters are used:

$$\mathbf{T_{meas}} = \mathbf{O_T}\mathbf{T_{MUT}}\mathbf{P_T} \tag{9}$$

where $\mathbf{O_T}$ and $\mathbf{P_T}$ are the T-parameters of the $\mathbf{O}$ and $\mathbf{P}$ matrices, and $\mathbf{T_{meas}}$ are the T-parameters obtained at the antenna terminals while assessing the MUT. The S-parameters corresponding to the MUT (the calibrated results) can be found by solving for $\mathbf{T_{MUT}}$ in Eq. (9), and transforming back to S-parameters. From the calibrated S-parameters, the dielectric properties can be estimated. The calibration and dielectric property estimation process is summarized in the flow chart of Figure 2, which will be illustrated through example first in simulations and then verified in measurement.

2.2. Performing Calibration in Simulation

The calibration method is first validated using a finite difference time domain (FDTD) simulation tool (SEMCAD X, SPEAG, Zurich). Simulations of the shielded UWB antennas have been shown to agree with measured results [13]. A pulse of center frequency 7 GHz and bandwidth 14 GHz is applied, and resulting S-parameters are extracted. Conversion from frequency domain to time domain is done using the inverse chirp Z-transform (iCZT).

The first step is to determine O_{11} and P_{22}, representing the reflections during each antenna's transmission. Two methods are possible in simulation. The first is to simulate one transmitting antenna with its aperture terminated with a perfectly-matched layer (PML). The second method is to use the two calibration simulations: the antennas separated by a PEC (Reflect), and the antennas directly in contact (Thru).

The two simulations performed for the second method provide a strong contrast in the reflected signal at the antenna aperture, as shown in Figure 3 at approximately 3 ns. The time of arrival of the signal at the antenna aperture is determined by subtracting Reflect and Thru and applying a threshold. A threshold of 10% of the maximum difference properly determines the aperture time. A Gaussian gate is then applied to isolate the reflected signal occurring before the aperture, which corresponds to reflections occurring within the antenna. The gate is described by:

$$w_{gate} = \begin{cases} 1, & \text{for } t < t_0 \\ e^{\frac{-(t-t_0)^2}{2\sigma^2}}, & \text{for } t > t_0 \end{cases} \tag{10}$$

where t_0 is the time determined by the subtraction method corresponding to the antenna aperture, and σ is the Gaussian root mean square width which is chosen to be 200 ps. This value is found to compromise between precision of aperture localization, and reduction of ripples in the frequency domain. O_{11} and P_{22} can then be determined in the time domain by multiplying w_{gate} by the time domain $Thru_{11}$ and $Thru_{22}$ signals, respectively. Thru signals are chosen rather than Reflect to avoid inclusion of strong reflections at the aperture.

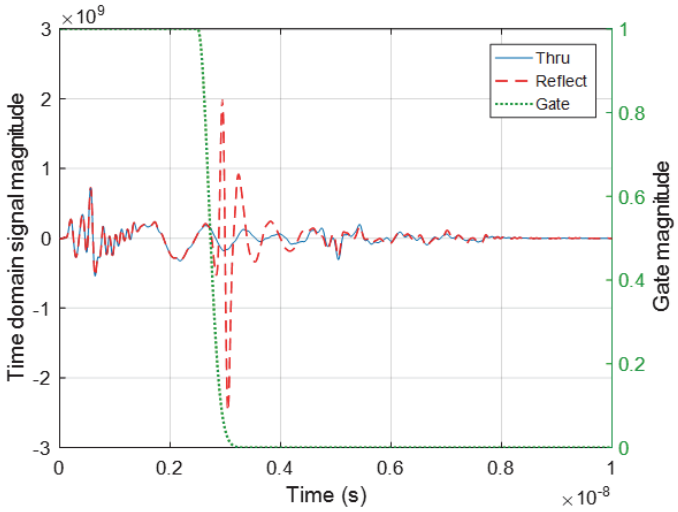

Figure 3. Time domain signal of the Reflect and Thru simulations, with the Gaussian gate used to isolate reflections due to the antenna.

A comparison between O_{11} obtained using the two methods is shown in the time domain in Figure 4 and the frequency domain in Figure 5. It can be seen that the PML method is able to account for reflections occurring after the antenna aperture, which are mostly low-frequency ringing. The majority of this ringing occurs below the operating band of the antennas, thus is not considered significant. The similarity between the two results validates the parameters chosen for the time domain gating. The time-gating method is used from this point onward since it is realizable in practice.

The O_{11} and P_{22} parameters are then de-embedded from the Thru and Reflect results. First, intermediate S-matrices for O and P are generated, consisting of:

$$\mathbf{O_{int}} = \begin{bmatrix} O_{11} & 1 \\ 1 & 0 \end{bmatrix}; \quad \mathbf{P_{int}} = \begin{bmatrix} 0 & 1 \\ 1 & P_{22} \end{bmatrix} \tag{11}$$

The de-embedded intermediate S-parameters are found using T-parameters, in the same method as in Eq. (9).

Using the quadratic formula in Eq. (8), the two solutions for O_{22} are obtained. The proper solution to the quadratic is clear considering O_{22} should be less than one for a passive antenna. P_{11} is then determined using Eq. (7), and is found to have similar values to O_{22}. The remaining parameters are then determined using Eqs. (1) and (2). All transmission parameters (O_{12}, O_{21}, P_{12}, and P_{21}) are nearly identical, which is expected for simulations.

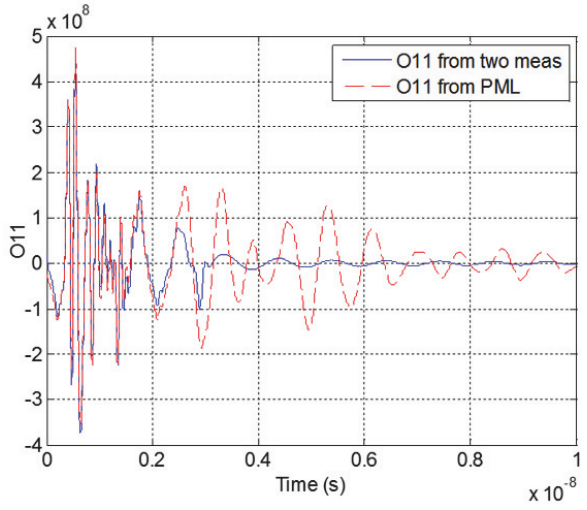

Figure 4. Time domain O_{11} obtained in simulation using the PML and two measurement methods.

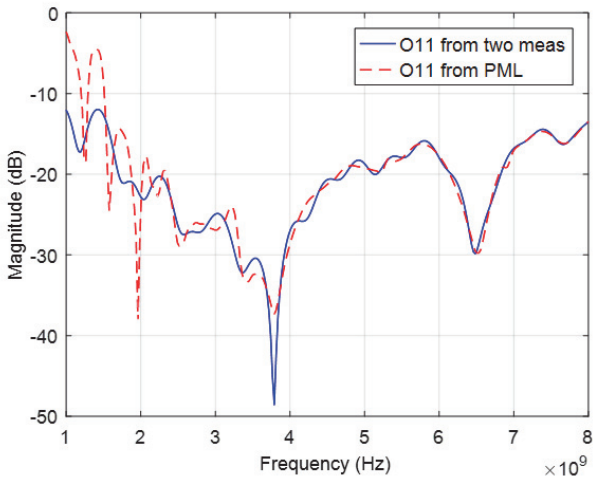

Figure 5. Frequency domain O_{11} obtained in simulation using the two methods.

As an example, the calibration method is applied to a simulation including a layer of material with muscle tissue properties. The 4-pole Cole-Cole model of muscle defined in [25] is fit to a single-pole Debye model, which can be represented in FDTD simulation. The tissue is modeled with 50 mm length (the separation distance between the antennas), 40 mm width, and 40 mm height. This configuration is shown in Figure 1(a)). Absorbing boundary conditions are placed at the edges of the muscle tissue to reduce effects such as multipath. In Figure 6, the calibrated S-parameters approach the theoretical S-parameters, which are calculated using uniform plane wave assumptions. The effects of calibration are clear in the time domain, as shown in Figure 7. The calibrated signal arrives much earlier since it corresponds only to the signal flight between the antenna apertures. It is also greater in amplitude due to compensation for the losses and reflections inherent in the antennas.

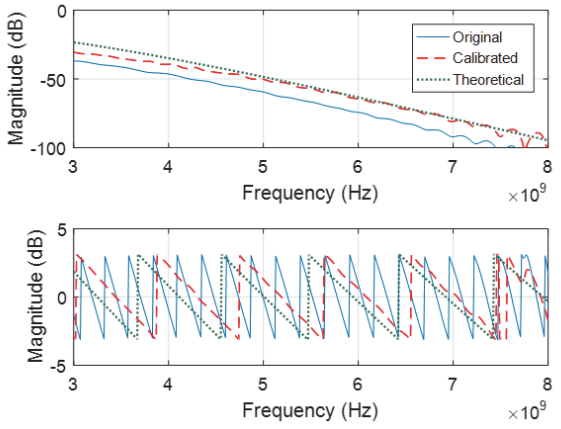

Figure 6. Magnitude and phase of the simulated, calibrated, and theoretical transmission coefficient S_{21} for muscle tissue.

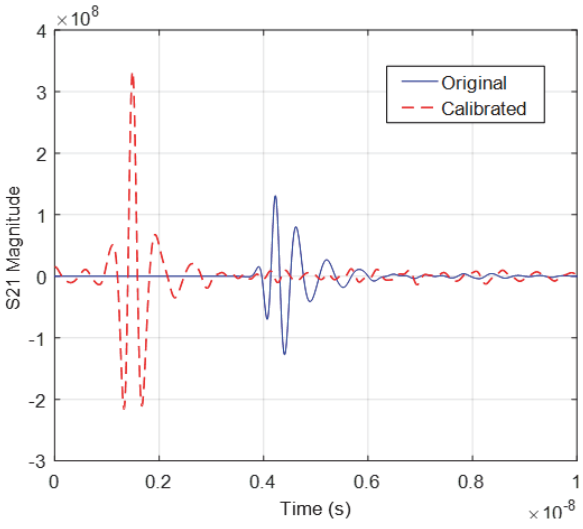

Figure 7. Original and calibrated time domain transmission coefficient S_{21} in simulation of muscle tissue assessment.

A procedure based on the Nicolson-Ross Weir (NRW) method [22] is then applied to estimate dielectric properties. The first step is to isolate the reflection at the interface of the antenna and the MUT. Next, the propagation factor is determined, and corrections are applied to phase and amplitude. Finally, permittivity and conductivity are estimated.

The reflection coefficient is isolated by modeling the multiple reflections and transmissions using a planar layered media model. Specifically, a planar region filled with the MUT is enclosed by regions containing the antenna dielectric filling (relative permittivity of approximately 25, and very low loss). Each material is treated as nonmagnetic ($\mu_{ant} = \mu_{MUT} = \mu_0$). Note that the MUT is not enclosed by a waveguide as in [22], so there is some spreading of the signal. Compensation for this is included later.

The reflection coefficient (Γ_{inf}) assuming an infinite sample length [22] is found from the calibrated reflection (S_{11}) and transmission (S_{21}) coefficients as:

$$\Gamma_{inf} = \chi \pm \sqrt{\chi^2 - 1} \tag{12}$$

where

$$\chi = \frac{S_{11}^2 - S_{21}^2 + 1}{2S_{11}} \tag{13}$$

The correct solution for Γ_{inf} can be found by considering that the magnitude of the reflection coefficient is bounded by 1 for passive materials. The propagation factor $e^{(-\gamma d)}$ can then be found from S_{11}, S_{21}, and Γ_{inf} as:

$$e^{-\gamma d} = \frac{S_{11} + S_{21} - \Gamma_{inf}}{1 - (S_{11} + S_{21})\Gamma_{inf}} \tag{14}$$

Next, the propagation constant $\gamma = \alpha + j\beta$ is estimated from the propagation factor $e^{(-\gamma d)}$ as:

$$\alpha_{est} = -\frac{\ln|e^{-\gamma d}|}{L}\,[\text{Np/m}] \tag{15}$$

$$\beta_{est} = -\frac{\arg(e^{-\gamma d})}{L}\,[\text{rad/m}] \tag{16}$$

where L is the distance between the antennas (occupied by the MUT). We then correct these terms because radial spreading causes a greater than expected attenuation constant α, and phase wrapping causes a phase ambiguity in estimating β.

A simple method is applied to account for the radial spreading of the transmitted signal. Since the radial spreading causes a loss in the signal intensity traveling through the tissue, an addition of signal magnitude is added per unit length. Through characterization in simulation, this addition is determined to be 1.2 dB/cm. Although the radial spreading depends on the tissue properties, frequency, separation distance, and antenna radiation pattern, this simple method is found to reasonably account for this spreading in a range of scenarios. Note that minor variation in this radial spreading term (e.g., 1.1 to 1.3 dB/cm) has little influence on the resulting property estimation, where changes less than 3% are observed.

Next, the unwrapped phase used to find β_{est} is offset from the true value by a nearly constant value as seen in Figure 8. This occurs because the antenna does not radiate below approximately 1.8 GHz. As in the NRW method, group delay is used to overcome this phase ambiguity. Group delay is estimated as:

$$\tau_{g,meas}(f) = -\frac{1}{2\pi}\frac{d\phi(f)}{df} \tag{17}$$

where $\phi(f)$ is the unwrapped phase of the estimated propagation factor $e^{(-\gamma d)}$. Group delay can also be calculated from estimated permittivity $\epsilon'_{r,est}$ and conductivity σ_{est} as:

$$\tau_{g,calc}(f) = L \cdot \text{Re}\left\{\frac{d}{df}\sqrt{\frac{\epsilon'_{r,est} - j\frac{\sigma_{est}}{\omega\epsilon_0}}{f^2\epsilon_0\mu_0}}\right\} \tag{18}$$

where permittivity and conductivity are estimated from the propagation constant as:

$$\epsilon'_{r,est} = \frac{\beta_{est}^2 - \alpha_{est}^2}{(2\pi f)^2 \epsilon_0 \mu_0} \tag{19}$$

$$\sigma_{est} = \frac{2\alpha_{est}\beta_{est}}{2\pi f \mu_0} \tag{20}$$

Next, the unwrapped phase $\phi(f)$ is linearly swept as:

$$\phi_\delta(f) = \phi(f) + \delta \tag{21}$$

where $\delta \in (-2n\pi : 0.01 : 2n\pi)$ rad, with n the maximum wavelengths expected in a sample (if unknown one can set this to a high number). Dielectric properties are estimated for each phase using Eqs. (19) and (20), and group delay is calculated in Eq. (18). The correct phase shift $\delta = k$ is chosen such that:

$$\tau_{g,meas}(f) - \tau_{g,calc,k}(f) \cong 0 \tag{22}$$

Prior to differentiating in Eqs. (17) and (18), the data is fit to second order polynomials to reduce the influence of noise. The corrected phase constant using the applied phase shift is shown in Figure 8, and is seen to closely resemble the theoretical value. Dielectric properties estimated using the complete procedure are shown in Figure 9. Very good agreement with the true values can be seen for both permittivity and conductivity, with average error of 3.94% and 4.71%, respectively.

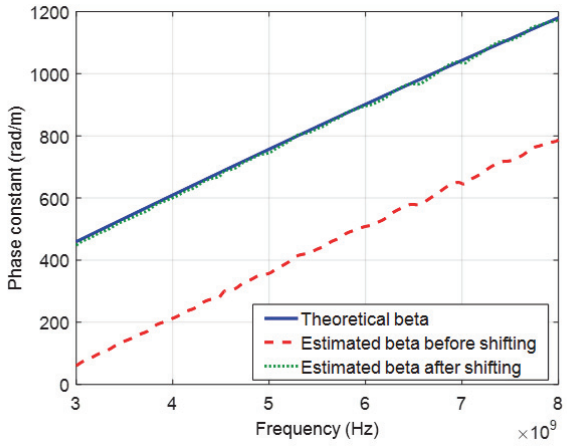

Figure 8. Estimated and theoretical phase constant for muscle tissue.

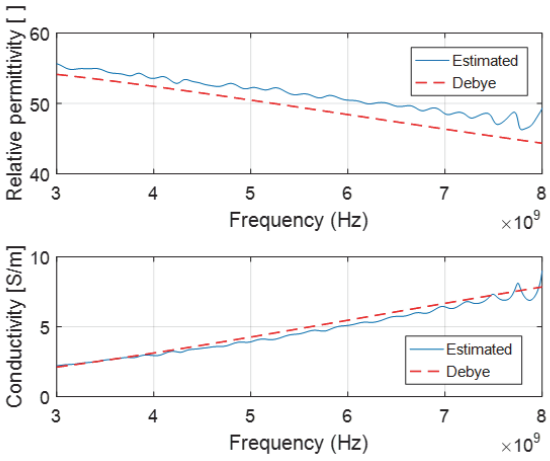

Figure 9. Estimated and literature dielectric properties of muscle [26] in simulation.

Note that the phase shift δ is not limited to multiples of 2π as in [22] because the reference planes after antenna calibration may not be precisely at the aperture. While the calibration procedures retain the signal within the waveguide of the antennas, tissue measurements include the transition from waveguide to MUT at the aperture. This transition modifies the signal phase at the antenna aperture by a small amount, particularly at frequencies close to the waveguide cutoff. A continuous phase sweep is thus found to better account for the phase ambiguity.

2.3. Performing Calibration in Measurement

The measurement system is shown in Figure 10. Two UWB antennas are mounted in a precise metal fixture where their separation distance can be controlled to within 0.01 mm using two thumbwheels. Measurements are recorded using a vector network analyzer (Agilent N5230A PNA-L). An intermediate frequency bandwidth of 100 Hz and a stimulus power of −2 dBm are used. The system is calibrated to the coaxial connections of the antennas using an electronic calibration unit (Agilent N4691A 3.5 mm Electronic Calibration Kit).

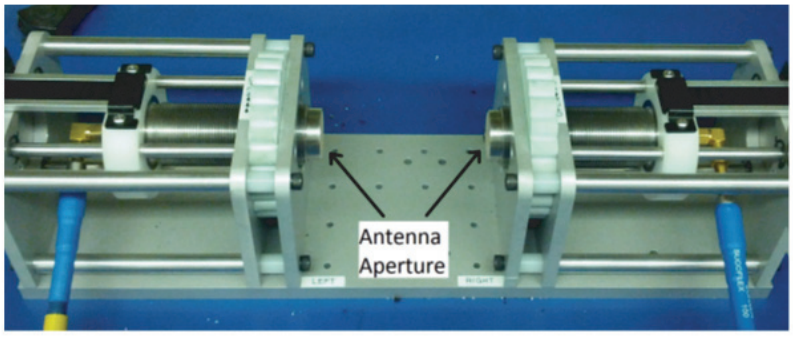

Figure 10. Measurement system consisting of two UWB antennas held in a metal fixture. The two thumbwheels are above the antenna apertures, and blue coaxial cables are connected to each antenna.

First, the Reflect calibration measurement is performed using a copper plate with a thin protecting plastic film. This film prevents unwanted resonances due to the metal antenna shielding in direct contact with a conductor, which are observed with a non-coated Aluminum sheet. Next, the Thru measurement is performed with the two antennas directly in contact with one another. The MUT is measured with the antennas adjusted to contact this material, then the calibration method is applied to the measured data. Here, we focus on the calibration parameters, specifically comparison with simulation. Property estimations are provided in the next section.

To determine O_{11} and P_{22}, time-gating is applied to the Reflect and Thru measurements. A comparison between O_{11} and P_{22} obtained from measurement and simulation is shown in Figure 11. Note that in simulation, since the models are ideal, O_{11} of the first antenna is equal to P_{22} of the second antenna, whereas in measurement there are slight manufacturing differences between the two antennas [13]. While the values do not align perfectly over the frequency range, the general trend is similar.

A similar comparison of O_{21} and P_{12} in simulation and measurement is shown in Figure 12. General agreement is again seen between the parameters, where precise agreement would not be expected due to manufacturing differences. The greater difference between simulated and measured O_{21} and P_{12} values with increasing frequency is likely due to a greater dispersion of the antenna dielectric loading in measurement than in simulation. This causes increased loss in measurements, resulting in lower O_{12}.

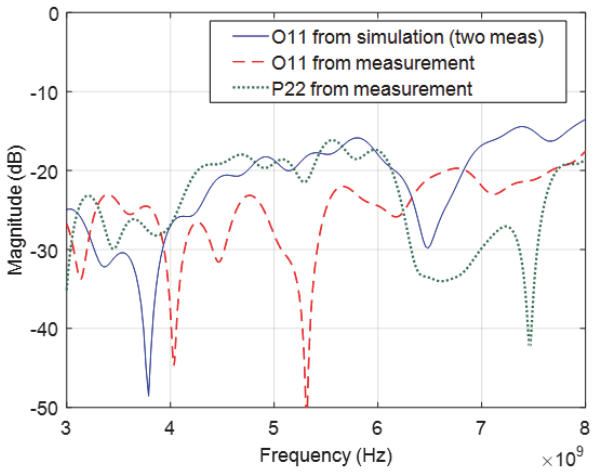

Figure 11. Comparison of O_{11} and P_{22} obtained from simulation (using the time-gating method) and measurement (note in simulation $O_{11} = P_{22}$).

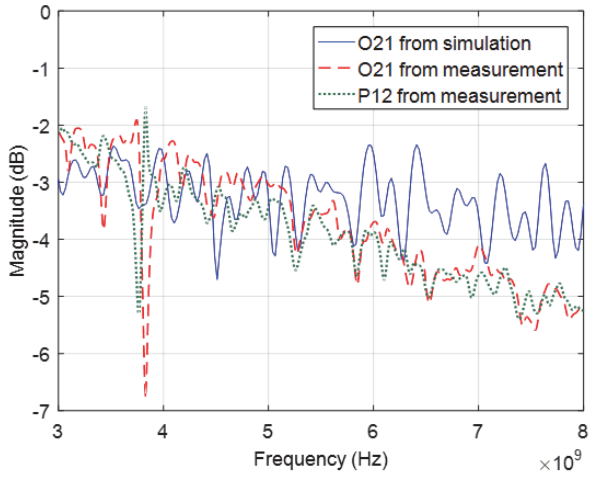

Figure 12. O_{21} and P_{12} in simulation and measurement ($O_{12} = O_{21}$ and $P_{12} = P_{21}$).

3. VALIDATION

To evaluate the performance of the calibration method with expected biological tissue properties, three mixtures described in [26] with similar properties to the healthy breast tissue groups defined in [27] are prepared using the surfactant Triton X-100, deionized water, and salt. Note that these are homogeneous mixtures used to validate the calibration technique. Future work will focus on property estimation of heterogeneous samples where reflections may occur within the sample. These mixtures are summarized in Table 1.

Table 1. Tissue-mimicking mixtures in deionized water solution.

Mixture	Triton X-100 concentration (% mass)	Salt concentration (% mass)
1	30	0.5
2	40	0.5
3	100	0

The open-ended coaxial probe described in [28], using the processing technique from [14], is used as a reference for estimations obtained from measurement. Single-pole Debye parameters are fit to the probe estimations using the criterion in [27], such that the properties can be modeled in simulation. The Debye parameters are given in Table 2.

Table 2. Debye parameters of the tissue-mimicking mixtures.

Mixture	Static permittivity ϵ_s [ ]	Optical permittivity ϵ_{inf} [ ]	Conductivity [S/m]	Relaxation time [ps]
1	47.77	13.44	0.0670	24.40
2	39.37	10.39	0.0577	26.24
3	4.70	2.87	0.0049	48.16

Antenna calibration is performed during each measurement session to account for temperature fluctuations which could affect antenna behavior. Liquids are enclosed in thin plastic bags during antenna measurements. These bags cause little effect on the results, as observed from the consistency of measurements of solid samples inside and outside the same bags. Estimated properties are given in Figures 13 to 15 in simulation and measurement at a 40 mm separation distance.

The average errors in simulation and measurement of each mixture at various separation distances representing expected tissue thicknesses are summarized in Table 3. Note that average errors are calculated over the usable frequency range, where the high loss mixtures are limited by the noise floor of the measurement equipment at high frequencies. The maximum frequency over which the error is calculated is noted below Table 3.

The majority of the estimated properties are accurate within 10%. Simulated results are generally very accurate, providing continued confidence in this method. It is important to note that probe estimations are used as a reference for the measured results. The probe is known to be accurate within approximately 10% [14], so the observed errors also include error from the probe estimations.

The largest errors are seen for the short separation distance measurements of the low permittivity Mixture 3. This error is likely due to the antennas' behavior in the near-field, since this sample presents a very short electrical length. Further, conductivity estimations of this mixture are seen to be challenging due to its very low loss. Measurements at larger separation distances of the lossy mixtures are also seen to be challenging. This is because of a narrower usable frequency range due to noise limitation.

Finally, we emphasize that the calibration is performed directly at the antenna aperture. Particularly for low frequencies, the antennas are operating in the near-field at this close proximity. This means that the antenna apertures may interact differently with the calibration procedures than during the tissue measurements, where a greater separation distance is given.

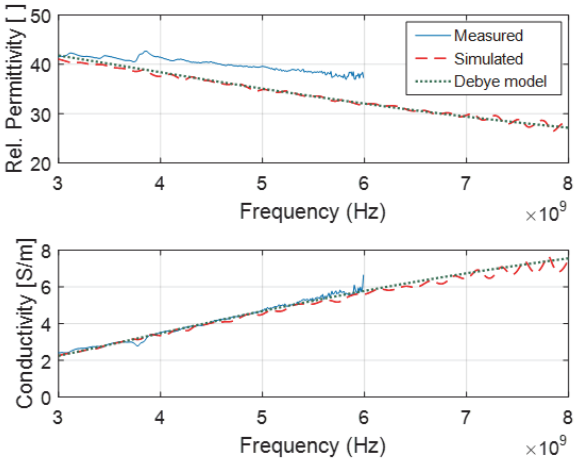

Figure 13. Estimated relative permittivity and conductivity of Mixture 1 in measurement and simulation at 40 mm separation distance.

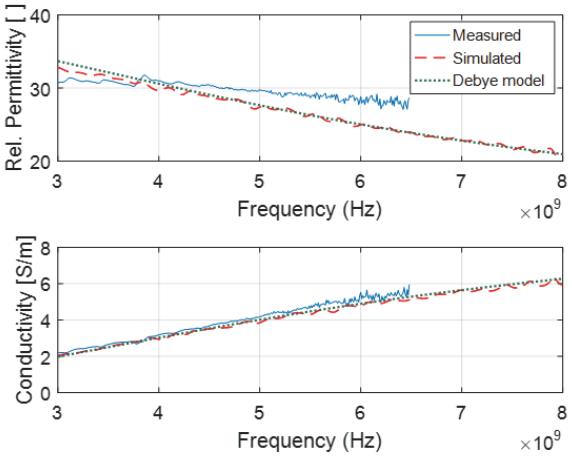

Figure 14. Estimated relative permittivity and conductivity of Mixture 2 in measurement and simulation at 40 mm separation distance.

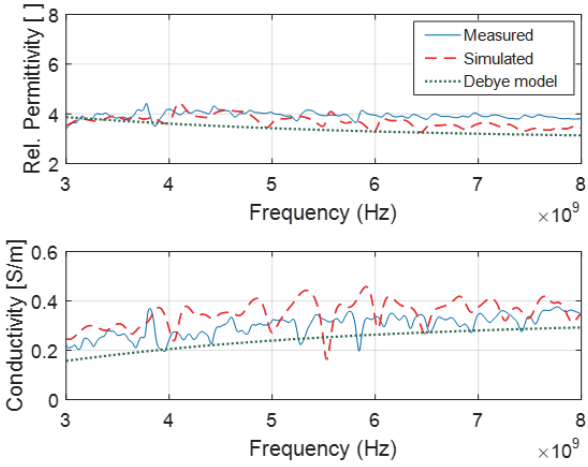

Figure 15. Estimated relative permittivity and conductivity of Mixture 3 in measurement and simulation at 40 mm separation distance.

4. ERROR ANALYSIS

To assess this method's response to uncertainties during measurements, error propagation from the measured parameters is analyzed using a technique similar to [29]. The parameters with uncertainty in this technique are the distance (recorded by the digital calipers), as well as the magnitude and phase of the reflection and transmission coefficients. The total error from each of these sources for the estimation of permittivity and conductivity is determined as:

$$\frac{\partial \epsilon'}{\epsilon'} = \frac{1}{\epsilon'}\sqrt{\left(\frac{\partial \epsilon'}{\partial L}\delta L\right)^2 + \sum_i \left[\left(\frac{\partial \epsilon'}{\partial |S_i|}\delta |S_i|\right)^2 + \left(\frac{\partial \epsilon'}{\partial \theta_i}\delta \theta_i\right)^2\right]} \tag{23}$$

$$\frac{\partial \sigma}{\sigma} = \frac{1}{\sigma}\sqrt{\left(\frac{\partial \sigma}{\partial L}\delta L\right)^2 + \sum_i \left[\left(\frac{\partial \sigma}{\partial |S_i|}\delta |S_i|\right)^2 + \left(\frac{\partial \sigma}{\partial \theta_i}\delta \theta_i\right)^2\right]} \tag{24}$$

Table 3. Average estimated dielectric property errors of the tissue-mimicking mixtures in simulation and measurement.

Mixture	Sep. Distance [mm]	Estimated permittivity error (%)		Estimated conductivity error (%)	
		Simulated	Measured	Simulated	Measured
1	30	1.10	9.56†	2.63	2.48†
	40	1.11	11.81*	2.56	3.04*
	50	1.79†	14.28*	1.90†	10.47*
2	30	2.36	11.03†	2.69	7.15†
	40	1.02	6.46†	1.82	4.70†
	50	1.15	14.64†	1.79	6.95†
3	30	24.30	40.72	58.92	50.53
	40	8.88	15.73	46.13	23.96
	50	6.09	7.60	39.57	4.89

* Maximum frequency of 6 GHz
† Maximum frequency of 7 GHz

where the subscript i corresponds to each of the S-parameters recorded for the tissue measurement, Thru, and Reflect, and θ denotes the phase of each S-parameter. Derivatives are calculated numerically by iteratively solving for the dielectric properties over a range of errors for each parameter. The parameter errors are as follows considering our measurement equipment: $\delta L = 0.1$ mm, $\delta|S_i| = 0.002$, $\delta\theta_{11} = \delta\theta_{22} = 3°$, and $\delta\theta_{12} = \delta\theta_{21} = 1°$. As an example, sources of error in the permittivity estimation of Mixture 1 are shown in Figure 16.

Error in the magnitude of the transmission coefficient in the MUT measurement $\delta|S_{(21,MUT)}|$ is generally seen to cause the greatest uncertainty in property estimation. Phase in the reflection coefficients in the MUT and Reflect measurement cause the next greatest uncertainty. Note that the transmission coefficients (S_{12} and S_{21}) of the Thru and Reflect procedures do not affect the property estimation due to the method's mathematical formulation. Examples of the total property estimation error for these parameter errors are shown in Figures 17 and 18, for Mixtures 1 and 3.

The largest uncertainty is generally seen at low frequencies, similar to [29]. A strong resonance is observed near 4 GHz, both in simulation and measurement. This is hypothesized to be due to the antenna shielding resonating, where it is approximately one wavelength long at this frequency.

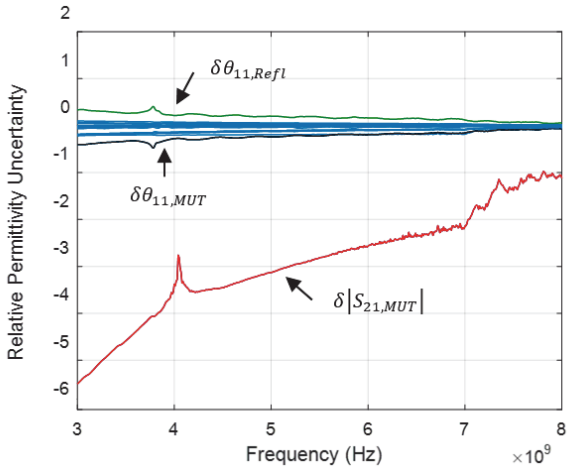

Figure 16. Uncertainty in the permittivity estimation of Mixture 1 due to each of the perturbed parameters, in measurement at 40 mm separation distance.

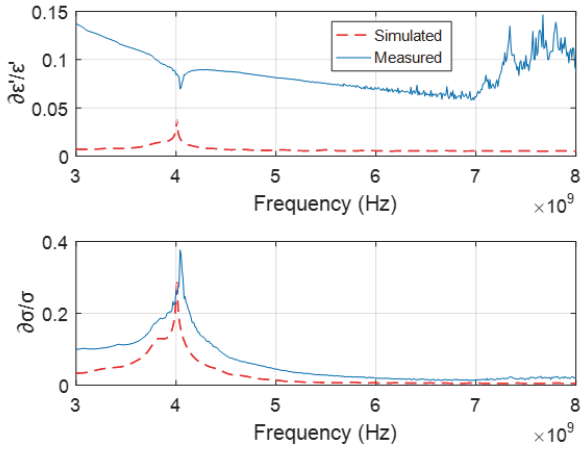

Figure 17. Total relative uncertainty of the permittivity and conductivity estimations of Mixture 1 in simulation and measurement.

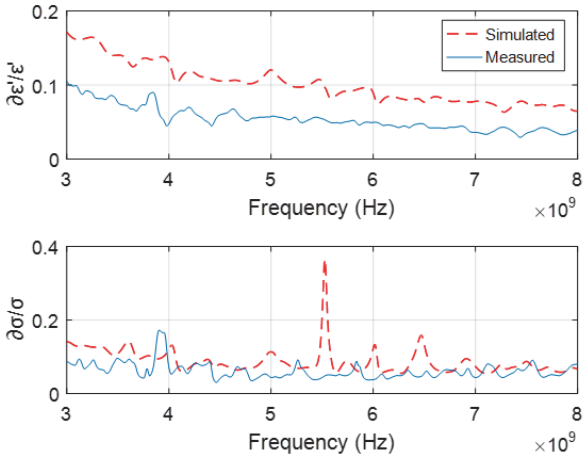

Figure 18. Total relative uncertainty of the permittivity and conductivity estimation of Mixture 3 in simulation and measurement.

This causes an effect similar to the Fabry-Pérot resonance often observed in transmission line material measurements [29]. Interestingly, this resonance is not observed in the simulated property estimations, but it is evident in the estimation uncertainty. This suggests a similar effect could occur in simulation, but it does not affect the resulting estimation to the same extent as in measurement.

The uncertainty in the permittivity estimation in measurement is greater than in simulation for Mixture 1, which is reflected by the greater error in measurement estimation (Table 3). Uncertainty is seen to be considerable for simulated and measured estimations of Mixture 3. However, this uncertainty is not as great as the property estimation errors summarized in Table 3. This is likely due to the radial spreading of the signal causing further error beyond the identified uncertainty in length and S-parameters.

5. CONCLUSION

A novel method of dielectric property estimation is developed for use with biological tissues, with the ultimate objective of assessing *in vivo* tissues. This technique is dubbed Gate Reflect Thru (GRT) due to its calibration procedures. Initial simulated and measured results for the estimation of dielectric properties are very promising despite the many challenges of near-field antenna property estimation. It is found that throughout much of the frequency range of these antennas, far-field approximations are applicable in estimating the properties. However, near-field antenna behavior is a significant consideration in developing this technique, and is particularly challenging for low permittivity materials.

Estimations generally lie within or near a 10% accuracy for mixtures representing homogeneous biological tissues at expected thicknesses. This method thus presents a convenient method for rapid estimation of dielectric properties as prior information for microwave imaging, and for quantitative tissue analysis. Further, this technique can likely be applied to many other antenna designs such as [30]. Criteria for applying other antennas include: sufficient bandwidth to resolve the antenna aperture in the time domain, limited mutual coupling between antennas when placed in contact with one another, and focused radiation. Applications such as agriculture sample property estimation [31] could also be explored with this technique, where less sample manufacturing is required compared with planar free space or transmission line measurements.

Future work involves implementing this technique in the 5×5 antenna array described in [12]. This will aid also in our microwave breast imaging system by providing an estimate of the background permittivity when reconstructing the images. The complex geometric spreading of the antenna will also be further investigated and characterized. Finally, we aim to implement this technique in smaller antennas for potential wearable applications.

ACKNOWLEDGMENT

The authors would like to thank the Natural Sciences and Engineering Council of Canada and Alberta Innovates Technology Futures for funding of this work.

REFERENCES

1. Nitz, W. R., A. Oppelt, W. Renz, C. Manke, M. Lenhart, and J. Link, "On the heating of linear conductive structures as guide wires and catheters in interventional MRI," *Journal of Magnetic Resonance Imaging*, Vol. 13, No. 1, 105–114, 2001.
2. Nagaoka, T., S. Watanabe, K. Sakurai, E. Kunieda, S. Watanabe, M. Taki, and Y. Yamanaka, "Development of realistic high-resolution whole-body voxel models of Japanese adult males and females of average height and weight, and application of models to radio-frequency electromagnetic-field dosimetry," *Physics in Medicine and Biology*, Vol. 49, No. 1, 1–15, 2003.
3. Garrett, J. D. and E. C. Fear, "Average dielectric property analysis of complex breast tissue with microwave transmission measurements," *Sensors*, Vol. 15, No. 1, 1199–1216, 2015.
4. Persson, M., A. Fhager, H. D. Trefná, Y. Yu, T. McKelvey, G. Pegenius, J.-E. Karlsson, and M. Elam, "Microwave-based stroke diagnosis making global prehospital thrombolytic treatment possible," *IEEE Transactions on Biomedical Engineering*, Vol. 61, No. 11, 2806–2817, 2014.
5. Meaney, P. M., D. Goodwin, A. H. Golnabi, T. Zhou, M. Pallone, S. D. Geimer, G. Burke, and K. D. Paulsen, "Clinical microwave tomographic imaging of the calcaneus: A first-in-human case study of two subjects," *IEEE Transactions on Biomedical Engineering*, Vol. 59, No. 12, 3304–3313, 2012.
6. Butterworth, I., J. Serallés, C. S. Mendoza, L. Giancardo, and L. Daniel, "A wearable physiological hydration monitoring wristband through multi-path non-contact dielectric spectroscopy in the microwave range," *2015 IEEE MTT-S 2015 International Microwave Workshop Series on RF and Wireless Technologies for Biomedical and Healthcare Applications (IMWS-BIO)*, 60–61, IEEE, 2015.
7. Irastorza, R. M., M. Mayosky, and F. Vericat, "Noninvasive measurement of dielectric properties in layered structure: A system identification approach," *Measurement*, Vol. 42, No. 2, 214–224, 2009.
8. Gabriel, S., R. W. Lau, and C. Gabriel, "The dielectric properties of biological tissues: II. Measurements in the frequency range 10 Hz to 20 GHz," *Physics in Medicine and Biology*, Vol. 41, No. 11, 2231–2249, 1996.
9. Gabriel, C, "Dielectric properties of biological tissue: Variation with age," *Bioelectromagnetics*, Vol. 26, No. S7, S12–S18, 2005.
10. Winters, D. W., J. D. Shea, P. Kosmas, B. D. Van Veen, and S. C. Hagness, "Three-dimensional microwave breast imaging: Dispersive dielectric properties estimation using patient-specific basis functions," *IEEE Transactions on Medical Imaging*, Vol. 28, No. 7, 969–981, 2009.
11. Chandra, R., H. Zhou, I. Balasingham, and R. M. Narayanan, "On the opportunities and challenges in microwave medical sensing and imaging," *IEEE Transactions on Biomedical Engineering*, Vol. 62, No. 7, 1667–1682, 2015.
12. Bourqui, J. and E. C. Fear, "System for bulk dielectric permittivity estimation of breast tissues at microwave frequencies," *IEEE Transactions on Microwave Theory and Techniques*, Vol. 64, No. 9, 3001–3009, 2016.
13. Bourqui, J. and E. C. Fear, "Shielded UWB sensor for biomedical applications," *IEEE Antennas and Wireless Propagation Letters*, Vol. 11, 1614–1617, 2012.
14. Popovic, D., L. McCartney, C. Beasley, M. Lazebnik, M. Okoniewski, S. C. Hagness, and J. H. Booske, "Precision open-ended coaxial probes for in vivo and ex vivo dielectric spectroscopy of biological tissues at microwave frequencies," *IEEE Transactions on Microwave Theory and Techniques*, Vol. 53, No. 5, 1713–1722, 2005.
15. Lavoie, B. R., M. Okoniewski, and E. C. Fear, "Estimating the effective permittivity for reconstructing accurate microwave-radar images," *PLOS One*, Vol. 11, No. 9, e0160849, 2016.

16. Engen, G. F. and C. A. Hoer, "Thru-reflect-line: An improved technique for calibrating the dual six-port automatic network analyzer," *IEEE Transactions on Microwave Theory and Techniques*, Vol. 27, No. 12, 987–993, 1979.
17. Ghodgaonkar, D. K., V. V. Varadan, and V. K. Varadan, "Free-space measurement of complex permittivity and complex permeability of magnetic materials at microwave frequencies," *IEEE Transactions on Instrumentation and Measurement*, Vol. 39, No. 2, 387–394, 1990.
18. Rolfes, I. and B. Schiek, "Calibration methods for microwave free space measurements," *Advances in Radio Science*, Vol. 2, No. A.1, 19–25, 2005.
19. Blackham, D. V., "Free space characterization of materials," *Antenna Measurement Techniques Association Symposium*, No. 15, 58–60, 1993.
20. Bartley, P. G. and S. B. Begley, "Improved free-space S-parameter calibration," *2005 IEEE Instrumentationand Measurement Technology Conference Proceedings*, Vol. 1, 372–375, IEEE, 2005.
21. Zhang, N., J. Cheng, G. Zhang, C. Cheng, and J. Liu, "A free-space measurement of complex permittivity in 8 GHz–40 GHz," *2014 Asia-Pacific Microwave Conference*, 849–851, IEEE, 2014.
22. Weir, W. B., "Automatic measurement of complex dielectric constant and permeability at microwave frequencies," *Proceedings of the IEEE*, Vol. 62, No. 1, 33–36, 1974.
23. Kanda, M., "Time domain sensors for radiated impulsive measurements," *IEEE Transactions on Antennas and Propagation*, Vol. 31, No. 3, 438–444, 1983.
24. Mason, S. J., *Feedback Theory: Further Properties of Signal Flow Graphs*, Research Laboratory of Electronics, Massachusetts Institute of Technology, 1956.
25. Gabriel, S., R. W. Lau, and C. Gabriel, "The dielectric properties of biological tissues: III. Parametric models for the dielectric spectrum of tissues," *Physics in Medicine and Biology*, Vol. 41, No. 11, 2271, 1996.
26. Henriksson, T., N. Joachimowicz, A. Joisel, C. Conessa, A. Diet, and J.-C. Bolomey, "Quantitative microwave breast phantom imaging using a planar 2.45 GHz system," *General Assembly of the International Union of Radio Science*, 1–4, 2008.
27. Lazebnik, M., M. Okoniewski, J. H. Booske, and S. C. Hagness, "Highly accurate Debye models for normal and malignant breast tissue dielectric properties at microwave frequencies," *IEEE Microwave and Wireless Components Letters*, Vol. 17, No. 12, 822–824, 2007.
28. Popovic, D. and M. Okoniewski, "Precision open-ended coaxial probe for dielectric spectroscopy of breast tissue," *2002 IEEE Antennas and Propagation Society International Symposium*, 815–818. IEEE, 2002.
29. Chalapat, K., K. Sarvala, J. Li, and G. S. Paraoanu, "Wideband reference-plane invariant method for measuring electromagnetic parameters of materials," *IEEE Transactions on Microwave Theory and Techniques*, Vol. 57, No. 9, 2257–2267, 2009.
30. Amineh, R. K., M. Ravan, A. Trehan, and N. K. Nikolova, "Near-field microwave imaging based on aperture raster scanning with TEM horn antennas," *IEEE Transactions on Antennas and Propagation*, Vol. 59, No. 3, 928–940, 2011.
31. Venkatesh, M. S. and G. S. V. Raghavan, "An overview of microwave processing and dielectric properties of agri-food materials," *Biosystems Engineering*, Vol. 88, No. 1, 1–18, 2004.